



Measurement report: Size-Resolved and Seasonal Variations in Aerosol Hygroscopicity Dominated by Organic Formation and Aging: Insights from a Year-Long Observation in Nanjing

Junhui Zhang¹, Yuying Wang¹, Jialu Xu¹, Xiaofan Zuo¹, Chunsong Lu¹, Bin Zhu¹, Yuanjian Yang¹, Xing Yan², Yele Sun³

¹State Key Laboratory of Climate System Prediction and Risk Management/Key Laboratory for Aerosol–Cloud Precipitation of China Meteorological Administration/Special Test Field of National Integrated Meteorological Observation, Nanjing University of Information Science & Technology, Nanjing 210044, China

²Faculty of Geographical Science, Beijing Normal University, Beijing 100875, China

³State Key Laboratory of Atmospheric Environment and Extreme Meteorology, Institute of Atmospheric Physics, Chinese Academy of Sciences, Beijing 100029, China

Correspondence to: Yuying Wang (yuyingwang@nuist.edu.cn)

Abstract: Aerosol hygroscopicity plays a significant role in atmospheric chemistry, radiation, and climate effects. While previous studies have investigated regional differences in aerosol hygroscopicity, long-term observational studies focusing on seasonal variations in specific regions remain scarce. This study explores size-resolved and seasonal variations in aerosol hygroscopicity in northern Nanjing, using one-year hygroscopicity-tandem differential mobility analyser (H-TDMA) measurements in 2021. Aerosols in the region show relatively low hygroscopicity due to a high organic mass fraction (annual average mass fraction: 42.92% in PM_{2.5}) in fine particles. The mean hygroscopicity parameter (κ_{mean}) increases with particle size across all seasons, with more pronounced size dependence in nucleation-mode particles. Particles (40–200 nm) show seasonal κ_{mean} variations: winter (0.12–0.24) and spring (0.14–0.25) display higher values attributable to secondary inorganic aerosols, while summer (0.12–0.21) and autumn (0.10–0.20) exhibit weaker hygroscopicity due to enhanced contributions from less hygroscopic components. Diurnal patterns are shaped by photochemical aging and aqueous-phase reactions, leading to κ_{mean} peaks for larger particles in the afternoon and evening. New particle formation events are most frequent in spring, producing initially less hygroscopic particles that become more hygroscopic with aging. Regional transport analysis reveals distinct controlling factors: hygroscopicity of nucleation-mode particles is mainly controlled by local sources, while accumulation-mode particles are more influenced by seasonal air mass transport. These results improve understanding of aerosol–cloud interactions and support regional climate modeling and air quality management in urbanizing areas.



1. Introduction

30 Aerosols, defined as mixtures of solid and liquid particles suspended in the atmosphere, possess hygroscopicity as a fundamental physicochemical property that governs their interactions with water vapor under varying environmental relative humidity (RH). This critical property, characterized by the particles' ability to absorb water, leads to a wide range of atmospheric impacts through complex mechanisms (Chen et al., 2019; Zhang et al., 2023).

Aerosol hygroscopicity plays a central role in determining the phase state, chemical reactions, optical properties, and cloud
35 nucleation activity of aerosol particles, thereby significantly influencing atmospheric chemistry, radiation, and climate effects (Chen et al., 2022; Peng et al., 2020; Ray et al., 2023; Swietlicki et al., 1999; Wang et al., 2025). Hygroscopic growth notably alters aerosol optical properties by modifying particle size distribution and refractive index, enhancing light scattering coefficient (Liu et al., 2022; Song et al., 2023). Furthermore, hygroscopicity promotes cloud formation by activating particles as cloud condensation nuclei, which leads to substantial changes in radiative forcing patterns (Rosenfeld et al., 2014;
40 Svenningsson et al., 2006). However, aerosol hygroscopicity is influenced by various factors, including environmental conditions and the physicochemical properties of aerosols, resulting in varying hygroscopicity across different environments (Gysel et al., 2007; Jiang et al., 2025).

Currently, multiple instruments and techniques are available for measuring aerosol hygroscopicity. Among the more established instruments are the hygroscopicity-tandem differential mobility analyser (H-TDMA), the cloud condensation
45 nuclei counter (CCNc), and the dual-nephelometer system (Chen et al., 2023; Jin et al., 2022; Song et al., 2023; Wang et al., 2017; Wang et al., 2023; Zhang et al., 2017). While these instruments can measure aerosol hygroscopicity, their measurement principles differ, and as a result, the resulting hygroscopicity data may show discrepancies (Liu et al., 2021; Liu et al., 2022; Ray et al., 2023; Zhang et al., 2017). Compared to other hygroscopicity measurement instruments, the H-TDMA, which is based on measuring particle number concentration, offers distinct advantages in studying the properties of ultrafine mode
50 particles (Wang et al., 2019). In addition to measuring the size-resolved hygroscopic growth factor (GF) of aerosols under varying relative humidity conditions, the H-TDMA can also provide insights into the mixing state of particles and reflect aerosol chemical compositions (Chen et al., 2022; Wang et al., 2018; Wang et al., 2019). According to Köhler theory, GF depends on chemical composition (Raoult effect) and particle size (Kelvin effect) (Petters and Kreidenweis, 2007). Compared with GF, hygroscopicity parameter (κ) introduced by Petters and Kreidenweis (2007) eliminates the influence of the Kelvin
55 effect, enabling direct comparison of hygroscopicity governed by the Raoult effect across different particle sizes (Kammermann et al., 2010; Petters and Kreidenweis, 2007).

A more profound understanding of aerosol hygroscopicity is crucial for improving the predictive capability of global climate models, particularly in simulating aerosol size distributions and their scattering properties under varying humidity conditions. The size dependence of aerosol hygroscopicity exhibits significant variations across different atmospheric environments (Peng
60 et al., 2020; Zhang et al., 2023). To better characterize the spatiotemporal evolution of aerosol hygroscopicity under diverse pollution conditions, extensive and comprehensive studies on its spatiotemporal variability are required. Furthermore,



understanding the effects of atmospheric processes, including new particle formation (NPF) and haze events, on aerosol hygroscopicity across heterogeneous environmental regimes remains imperative (Chen et al., 2022).

65 NPF, defined as the evolution process where newly formed sub-3 nm particles grow to larger sizes, represents a significant atmospheric aerosol source capable of influencing aerosol hygroscopicity and has been observed globally (Hirshorn et al., 2022; Shen et al., 2023; Yli-Juuti et al., 2011). Generally, freshly nucleated particles exhibit lower hygroscopicity, and the hygroscopicity increases with particle aging (Asmi et al., 2010). NPF events dominated by different chemical components exert distinct impacts on aerosol hygroscopicity. Newly formed sulfate-dominated particles exhibit higher hygroscopicity, whereas organics-dominated counterparts display lower hygroscopicity (Hong et al., 2024; Ma et al., 2016). However, Liu et al. (2021) observed that on NPF events, photochemical oxidation triggered by the nucleation of volatile organic compounds
70 generates more water-soluble organic acids, resulting in higher hygroscopicity of organic aerosols on NPF days compared to non-NPF days.

In recent years, numerous studies on aerosol hygroscopicity based on H-TDMA observation data have been conducted globally. It has been found that the probability density function of GF or κ (GF/ κ -PDF) exhibits a bimodal distribution at urban sites
75 (Shi et al., 2022; Spitieri et al., 2023; Tan et al., 2013; Wang et al., 2018), while at some non-urban sites, it shows a unimodal or quasi-unimodal distribution (Chen et al., 2022; Wang et al., 2018). Wang et al. (2019) discovered that nucleation-mode particles during clean periods mainly originate from nucleation events followed by growth, whereas during severe pollution periods, they predominantly come from primary emissions in urban environments. Conversely, accumulation-mode particles are primarily from primary emissions during clean periods and secondary processes during pollution periods, resulting in
80 notable differences of aerosol hygroscopicity for different mode particles under varying pollution levels. Additionally, aerosol hygroscopicity exhibits substantial differences among air masses of varying origins. Over the Antarctic continent, dry continental air masses are reported to exhibit stronger hygroscopicity than moist marine air masses (Asmi et al., 2010). At an urban site in Beijing, seasonal hygroscopicity variations are strongly correlated with air mass source regions (Zhang et al., 2023).

85 Aerosol concentration and composition undergo significant variations on both temporal and spatial scales. Long-term measurements of aerosol hygroscopicity are crucial for understanding its seasonal and annual variations, as well as its impacts on visibility, atmospheric chemistry, and climate change (Peng et al., 2020). In some regions of the world, studies utilizing H-TDMA for long-term measurements of aerosol hygroscopicity have already been conducted (Alonso-Blanco et al., 2019; Fors et al., 2011; Kammermann et al., 2010; Mamali et al., 2018; Ray et al., 2023). These observations reveal that aerosol
90 hygroscopicity is highly depending on their sources and physicochemical aging processes. In China, numerous observational experiments measuring aerosol hygroscopicity using H-TDMA have been carried out in regions such as the North China Plain (NCP), the Yangtze River Delta (YRD), and the Pearl River Delta (PRD) (e.g., Jiang et al., 2016; Jiang et al., 2025; Wang et al., 2017). However, most measurements limit to short-term field campaigns (typically 1–2 months duration), which makes it impossible to determine the seasonal variations and their factors in aerosol hygroscopicity at specific locations (Fan et al.,
95 2020).



In this study, the H-TDMA system is utilized in the northern suburbs of Nanjing to obtain size-resolved hygroscopicity observation data for submicron aerosols, covering the entire year from January to December 2021. The H-TDMA observations enable the determination of size-resolved and seasonal variations in aerosol hygroscopicity in the Nanjing region and further facilitate the analysis of influencing factors contributing to these hygroscopicity differences. This paper is structured as follows. Section 2 describes the instrumentation and the methods to data analysis. Aerosol hygroscopicity during different seasons are discussed in Sect. 3. Conclusions and summary are given in Sect. 4.

2. Experiment and data analysis

2.1. Measurement site and campaign

A comprehensive field observation experiment was conducted in the northern suburbs of Nanjing in 2021, aiming to delve deeply into the interactions among the atmosphere, aerosol, boundary layer, and cloud interactions. The observation site is located on the campus of Nanjing University of Information Science and Technology (NUIST, 32°13' N, 118°46' E) in the northern suburban area of Nanjing, which is situated in the central YRD. Further details on the field campaign and measurement site are available in Song et al. (2023).

This work provides a comprehensive examination of seasonal variations in aerosol hygroscopicity and their relationship with chemical composition, based on year-round observational data collected from January to December 2021. The dataset is partitioned according to conventional meteorological seasons: winter (Jan–Feb and Dec 2021), spring (Mar–May 2021), summer (Jun–Aug 2021), and autumn (Sep–Nov 2021).

2.2. Measurements and data analysis

2.2.1. Measurement of aerosol hygroscopicity

The H-TDMA used in this study primarily consists of two differential mobility analysers (DMA, Model 3081L, TSI Inc.) and a condensation particle counter (CPC, Model 3772, TSI Inc.). The dried and neutralized aerosol sample is first passed through the first DMA, which selects monodisperse particles of specific diameters (40, 80, 110, 150, and 200 nm). Subsequently, the sample with monodisperse particles is humidified to RH=90% via a nafion humidifier. Finally, the sample is directed through the second DMA and the CPC to measure the particle number size distribution of the humidified particles.

The hygroscopic growth factor (GF) is defined as:

$$GF = \frac{D_p(RH)}{D_p(dry)}, \quad (1)$$

where $D_p(dry)$ denotes the dry diameter of monodisperse particles selected by the first DMA before humidification, and $D_p(RH)$ represents the particle diameter selected by the second DMA after humidification at RH = 90%.



The H-TDMA data can be used to compute the measured distribution function of GF for any selected D_p (dry) particles, which is then used to retrieve the probability distribution function of GF (GF-PDF) according to the multi-mode TDMAfit algorithm. The hygroscopicity parameter (κ) is calculated as follows (Petters and Kreidenweis, 2007):

$$\kappa = (GF^3 - 1) \cdot \left[\frac{1}{RH} \exp \left(\frac{4 \sigma_{s/a} M_w}{R T \rho_w D_p GF} \right) - 1 \right], \quad (2)$$

where $\sigma_{s/a}$ is the surface tension of the droplet–air interface at the composition of the droplet, M_w is the molar mass of water, R is the universal gas constant, T is the temperature, and ρ_w is the density of water.

The probability distribution function of κ (κ -PDF, $c(\kappa, D_p)$) derived from GF-PDF is normalized by $\int c(\kappa, D_p) d\kappa = 1$. Based on the κ values, aerosol particles are categorized into three hygroscopic groups: nearly hydrophobic (NH, $\kappa < 0.1$), less hygroscopic (LH, $0.1 \leq \kappa < 0.2$), and more hygroscopic (MH, $\kappa \geq 0.2$). The MH groups mainly consist of inorganic species such as sulfates, nitrates, and ammonium salts. In contrast, the NH and LH groups are primarily composed of black carbon, insoluble organics, and partially soluble organics (Liu et al., 2011; Müller et al., 2017).

The mean κ (κ_{mean}) is then defined as the number-weighted mean of κ -PDF over the κ range $[a, b]$:

$$\kappa_{\text{mean}} = \int_a^b \kappa c(\kappa, D_p) d\kappa, \quad (3)$$

where a and b represent the lower and upper integration limits of κ . For the ensemble κ_{mean} , the integral spans the entire domain, i.e., $a = 0$ and $b \rightarrow \infty$. When computing κ_{mean} of NH, LH, and MH hygroscopic groups (κ_{NH} , κ_{LH} , and κ_{MH}), a and b are set according to the predefined κ range of each group.

Accordingly, the number fraction (NF) for each hygroscopic group with over the range $[a, b]$ is defined as:

$$NF = \int_a^b c(\kappa, D_p) d\kappa. \quad (4)$$

The standard deviation of κ -PDF ($\sigma_{\kappa\text{-PDF}}$) is calculated as:

$$\sigma_{\kappa\text{-PDF}} = \left(\int_0^\infty (\kappa - \kappa_{\text{mean}})^2 c(\kappa, D_p) d\kappa \right)^{\frac{1}{2}}. \quad (5)$$

Previous research has widely adopted $\sigma_{\kappa\text{-PDF}}$ as a metric for aerosol mixing state characterization (Jiang et al., 2016; Wang et al., 2017). However, this absolute dispersion parameter fails to account for scenarios where significant κ_{mean} variations exist between different sizes. To address this limitation, this study introduces the coefficient of variation ($CV_{\kappa\text{-PDF}}$):

$$CV_{\kappa\text{-PDF}} = \frac{\sigma_{\kappa\text{-PDF}}}{\kappa_{\text{mean}}}. \quad (6)$$

This normalized parameter effectively captures the relative dispersion of size-resolved κ -PDF by incorporating κ_{mean} differences among particle populations. Consequently, $CV_{\kappa\text{-PDF}}$ serves as the primary mixing state indicator in this study, with lower values corresponding to stronger internal mixing.



2.2.2. Measurements of other aerosol properties

The measurement of aerosol chemical compositions is conducted using an aerosol chemical speciation monitor (ACSM, Aerodyne Research Inc.) coupled with an aethalometer (AE-33, Magee Scientific Inc.). Both instruments are configured with PM_{2.5} sampling inlets: the ACSM system incorporates a PM_{2.5} aerodynamic lens, while the AE-33 utilizes an aerosol cutter with 2.5 µm cutoff diameter. This configuration ensures measurement of particulate matter mass concentrations specifically for the aerodynamic diameter fraction below 2.5 µm (PM_{2.5}).

The ACSM operates at a temporal resolution of 15 minutes, while the AE-33 provides measurements at a higher resolution of 1 minutes. The ACSM, equipped with a capture vaporizer and a quadrupole mass spectrometer, is primarily used to measure the mass concentrations of organic aerosols (OA), sulfate (SO₄²⁻), nitrate (NO₃⁻), ammonium (NH₄⁺), and chloride (Cl⁻). To further analyse OA composition, the positive matrix factorization analysis is applied to differentiate between primary organic aerosols (POA) and secondary organic aerosols (SOA). Concurrently, the AE-33 is employed to measure the mass concentration of black carbon (BC). The total PM_{2.5} mass concentration is derived by summing the mass concentrations of all components measured by the ACSM and AE-33. The absence of dust-related measurements may lead to underestimation of PM_{2.5} mass concentrations during dust episodes in this study.

The particle number size distribution (PNSD) is measured by two scanning mobility particle sizers (SMPS) covering different size ranges: Nano-SMPS (2–60 nm) and SMPS (15–700 nm), both operating with a temporal resolution of 5 minutes. The Nano-SMPS is specifically used for auxiliary identification of NPF events. Particles are classified into two modes based on their diameter: nucleation mode ($D_p \leq 100$ nm) and accumulation mode ($100 \text{ nm} < D_p \leq 700$ nm). Then the total number concentrations in nucleation and accumulation modes (N_{nuc} and N_{acc}) are then calculated.

2.3. Backward trajectory calculation and clustering analysis

Backward trajectories of air masses arriving at the sampling site are calculated using the NOAA HYSPLIT-4 (Hybrid Single-Particle Lagrangian Integrated Trajectory) model (Draxler and Hess, 1998; Wu et al., 2016). The 72-hour backward trajectories are initiated at 3-hour intervals from 00:00 to 21:00 LT (Local Time, UTC+08) and terminated at 100 m above ground level. The number of clusters is determined based on the variation in total spatial variance (refer to the HYSPLIT4 User Guide), with the k-means clustering algorithm applied to classify trajectories for each season. To balance optimal trajectory separation (favoring a larger number of clusters) with visualization simplicity (preferring fewer clusters), air mass backward trajectories are partitioned into 3 clusters per season.



3. Results and discussion

3.1. Overview

3.1.1. Seasonal variations of size-resolved aerosol hygroscopicity

As shown in Figure 1a, a significant increase in κ_{mean} with particle size is observed in all seasons, consistent with a previous study in Nanjing (Jiang et al., 2025). The size-resolved annual κ_{mean} values are 0.12 ± 0.04 , 0.16 ± 0.05 , 0.18 ± 0.05 , 0.20 ± 0.05 , and 0.22 ± 0.06 for particles with diameters of 40, 80, 110, 150, and 200 nm, respectively (Table S1). Similar hygroscopicity-particle size dependence is observed in Madrid, while more complex relationships are found in Athens, India and Switzerland (Alonso-Blanco et al., 2019; Spitieri et al., 2023; Ray et al., 2023; Kammermann et al., 2010). The enhancement of aerosol hygroscopicity with particle size may be attributed to chemical aging processes of particles and an increased proportion of inorganic components (Alonso-Blanco et al., 2019; Wu et al., 2016). Compared to the measurements in the NCP (Chen et al., 2022), κ at this site is significantly lower, likely due to the dominance of organic aerosols (annual average mass fraction: 42.92% in $\text{PM}_{2.5}$) (Figure 1b). This pattern closely resembles observations from Shanghai, which is also located within the YRD region (Chen et al., 2022).

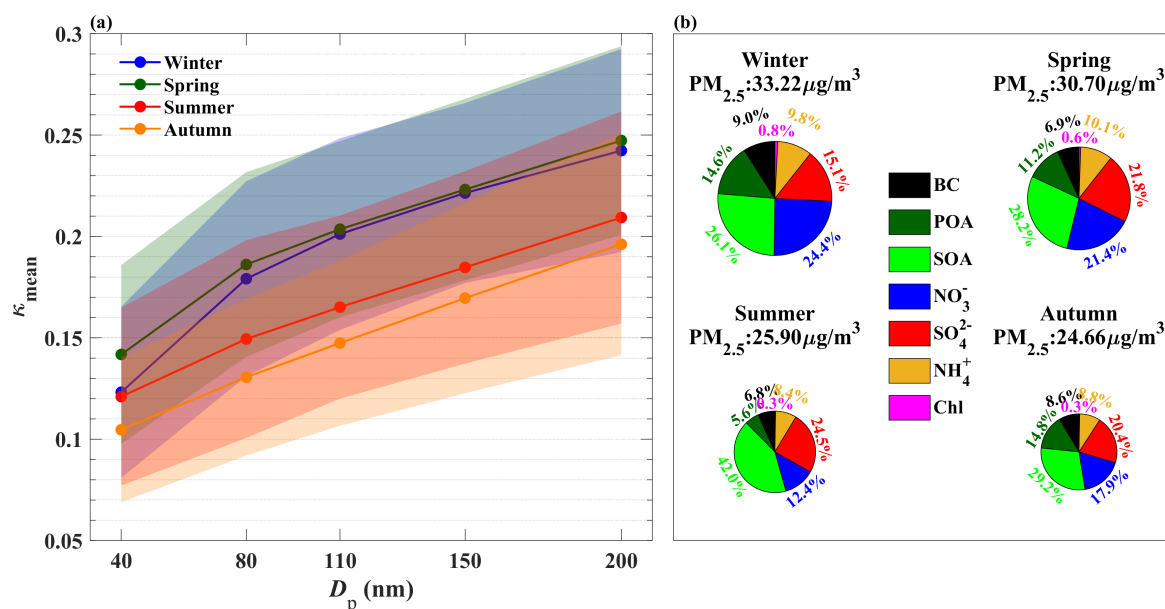


Figure 1. (a) Size variations of the mean hygroscopicity parameter (κ_{mean}) during different seasons, with error bands indicating the standard deviations of κ_{mean} . (b) Seasonal distributions of mass concentrations and compositional fractions for $\text{PM}_{2.5}$ chemical species.



A pronounced seasonal contrast in κ_{mean} is observed for 40 nm particles, with spring exhibiting the highest value ($\kappa_{\text{mean}} = 0.14$) compared to other seasons ($\kappa_{\text{mean}} = 0.10\text{--}0.12$). For larger particles (80–200 nm), obviously higher κ_{mean} values are recorded in winter and spring than in summer and autumn. This pattern may be attributed to the increased mass fractions of more hygroscopic sulfate–nitrate–ammonium (SNA) during the more severe PM_{2.5} pollution in winter and spring. As shown in Figure 1b, the mass concentrations of PM_{2.5} during winter and spring exceed 30 $\mu\text{g m}^{-3}$, with corresponding higher MF_{SNA} (the mass concentration of SNA, MF_{SNA}) values of 49.37% and 53.25%, respectively. In contrast, summer and autumn measurements show lower PM_{2.5} levels, averaging approximately 25 $\mu\text{g m}^{-3}$, with corresponding lower MF_{SNA} values of 45.33% and 47.13%, respectively. Similar seasonal variation patterns in aerosol chemical composition are reported at another site in Nanjing during 2016–2017 (Xie et al., 2022).

Figure 1a also suggests that nucleation-mode particles (40 and 80 nm) display greater size-dependent κ_{mean} variability than accumulation-mode particles (110, 150, and 200 nm), particularly during winter and spring. This is likely due to the higher organic content in nucleation-mode particles, especially in winter and spring. Consequently, the κ_{mean} increase rate with particle size is substantially steeper across the nucleation mode than the accumulation mode size range.

In summary, aerosols in the northern suburban area of Nanjing exhibit relatively low hygroscopicity, primarily due to their elevated organic content. A consistent increase in hygroscopicity with particle size is observed across all seasons, with this trend being particularly pronounced for nucleation-mode particles (40–80 nm). Furthermore, aerosols in winter and spring demonstrate enhanced hygroscopicity in the 40–200 nm size range compared to summer and autumn, which can be attributed to higher concentrations of SNA.

3.1.2. Seasonal variations of hygroscopic groups in the different size particles

Figure 2a illustrates the seasonal variations in the NF and κ of different hygroscopic groups (NH, LH, MH) across various particle sizes. With the exception of 40 nm particles, the size variations in κ_{NH} and κ_{LH} are less pronounced than those of κ_{MH} . Meanwhile, NF_{MH} shows a notable increase with particle size. Considering the increase of κ_{mean} with particle size (Figure 1a), this phenomenon suggests that the size variation in κ_{mean} is mostly driven by MH group particles. Unlike particles in other size ranges, the 40 nm particles have relatively small seasonal differences in κ_{NH} , κ_{LH} , and κ_{MH} . The κ_{mean} of 40 nm particles in spring is much higher than in other seasons due to the lower NF_{NH} and higher NF_{MH} of 40 nm particles.

For nucleation-mode particles, κ_{NH} is found to increase consistently from winter and spring to summer and autumn, whereas for accumulation-mode particles, the lowest κ_{NH} values are recorded during summer. However, the variation in κ_{NH} remains minor, generally within the range of 0.03–0.05. In contrast, κ_{LH} for nucleation-mode particles is slightly higher in spring compared to other seasons, while for accumulation-mode particles, it reaches slightly higher values in summer. Despite these variations, κ_{LH} remains stable, typically ranging between 0.14–0.17, which is in the κ range of SOA (Petters and Kreidenweis, 2007). Across all particle sizes, both κ_{MH} and NF_{MH} are bigger in winter and spring than in summer and autumn for the same particle sizes. Considering the higher κ_{mean} in winter and spring compared to summer and autumn (Figure 1a), this suggests that the seasonal in κ_{mean} is likely driven by MH group particles.



In general, aerosol particles in winter exhibit higher κ_{MH} compared to spring likely due to their greater abundance of NO_3^- , which possesses stronger hygroscopicity. This effect is particularly evident in accumulation-mode particles, which displays a more pronounced seasonal contrast. However, a significantly higher NF_{MH} is observed in spring compared to winter due to the greater abundance of SNA, leading to an increased κ_{mean} in spring (Figure 1). Although the differences in aerosol κ_{MH} between summer and autumn are relatively small, the higher NF_{MH} in summer results in greater κ_{mean} across all particle size ranges.

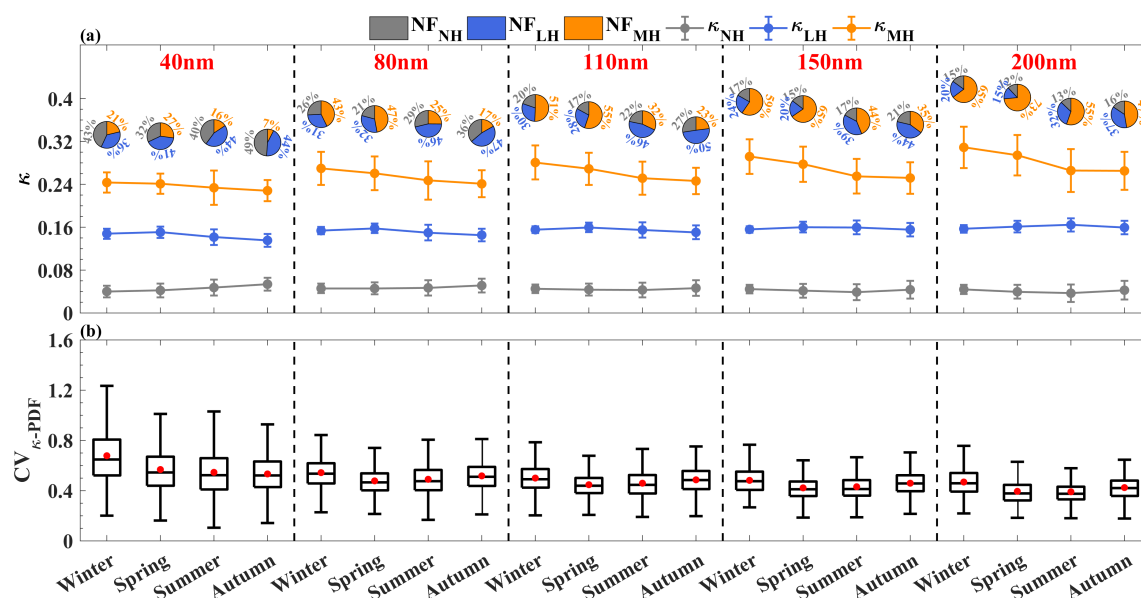


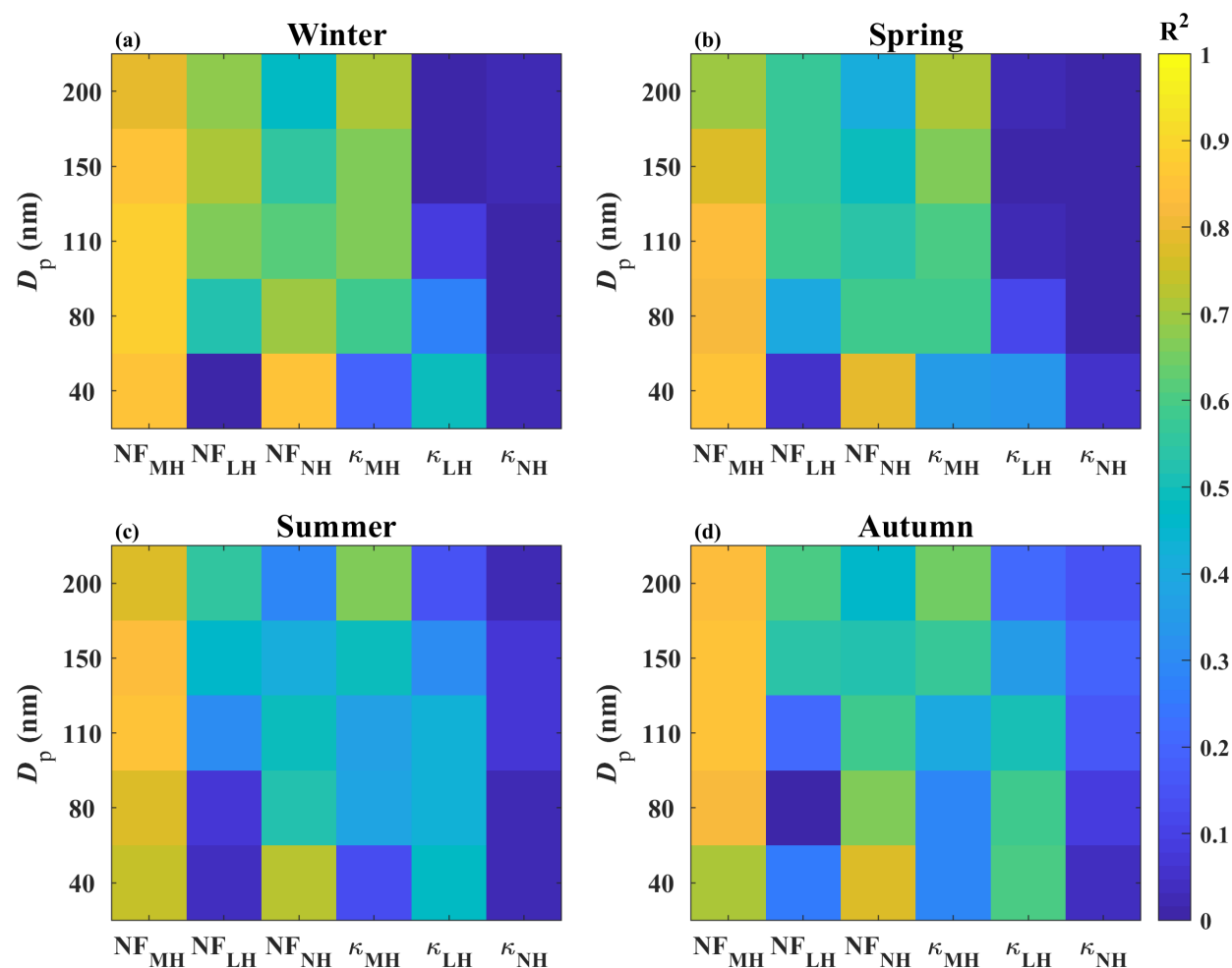
Figure 2. (a) Seasonal variations of NF_{MH} , NF_{LH} , and NF_{NH} (represented by orange, blue, and gray segments in the pie charts, respectively), alongside the corresponding κ_{MH} , κ_{LH} , and κ_{NH} (represented by orange, blue, and gray lines) for different size particles (40–200 nm). Error bars indicate the standard deviation of each parameter. (b) Seasonal variations of $\text{CV}_{\kappa\text{-PDF}}$ for different size particles. Boxplots display the mean (red dots), interquartile range (25th–75th percentiles), and 5th–95th percentile ranges.

Figure 2b demonstrates a consistent inverse relationship between $\text{CV}_{\kappa\text{-PDF}}$ and particle size across all seasons, reflecting enhanced internal mixing during aerosol aging and growth processes. Notably, nucleation-mode particles exhibit significantly higher $\text{CV}_{\kappa\text{-PDF}}$ values in winter compared to other seasons, suggesting a more pronounced external mixing state. This seasonal pattern likely results from reduced photochemical activity during winter months, which inhibits atmospheric aging processes and promotes the persistence of externally mixed aerosols.

To further elucidate the impact of different hygroscopic groups on κ_{mean} , the correlation coefficients (R^2) between the κ_{mean} and six parameters (NF_{MH} , NF_{LH} , NF_{NH} , κ_{MH} , κ_{LH} , and κ_{NH}) are calculated (Figure 3). The results indicate that κ_{mean} is predominantly influenced by NF_{MH} in all seasons. For nucleation-mode particles, κ_{mean} is also affected largely by NF_{NH} , particularly for 40 nm particles, where the R^2 between NF_{NH} and κ_{mean} (0.76–0.89) is even slightly higher than that between



250 NF_{MH} and κ_{mean} (0.66–0.88). This phenomenon can be attributed to the fact that nucleation-mode particles, primarily originating from direct emissions or NPF events with limited aging, are typically composed of more hydrophobic matters (e.g., OA and BC) (Gysel et al., 2007; Li et al., 2023). These particles are characterized by higher NF_{NH} and lower NF_{MH} , leading to NF_{NH} being a dominant factor in determining κ_{mean} for nucleation-mode particles.



255 **Figure 3. The correlation coefficients (R^2) between κ_{mean} and six parameters (NF_{MH} , NF_{LH} , NF_{NH} , κ_{MH} , κ_{LH} , κ_{NH}) for different size particles (40–200 nm) during different seasons.**

260 Furthermore, these findings suggest that variations in the NF of different hygroscopic groups have a greater impact on κ_{mean} than variations in the κ values of these groups. Beyond the influence by the NF of different hygroscopic groups, κ_{mean} for accumulation-mode particles is also significantly affected by κ_{MH} , while for nucleation-mode particles, due to their relatively



weaker hygroscopicity, κ_{mean} is jointly influenced by κ_{MH} and κ_{LH} . Compared to winter and spring, the influence of κ_{MH} on κ_{mean} is smaller in summer and autumn, whereas the influence of κ_{LH} on κ_{mean} is greater. This pattern is attributed to the κ_{mean} across different particle sizes is lower in summer and autumn than in winter and spring.

3.1.3. Seasonal variation of diurnal cycles in aerosol hygroscopicity

As illustrated in Figure 4a1–a4, rush-hour-induced enhancements of particle number concentration demonstrate distinct seasonal variability, with particularly pronounced effects on nucleation-mode particles during morning (~06:00 LT) and evening (~20:00 LT) periods. The phenomenon attains its maximum intensity during winter and spring seasons, periods that frequently coincide with atmospheric stagnation events. Quantitative analysis reveals substantial PM_{2.5} mass accumulation during rush hours across all non-summer seasons, accompanied by synchronous increases in both BC mass concentrations and fractions (M_{BC} and MF_{BC}) (Figure 4). These traffic-induced compositional changes in rush hours drive systematic reductions in κ_{mean} values across all particle size ranges due to increased NF_{NH} (Figure 5). Notably, the suppression effect on particle hygroscopicity exhibits its greatest sensitivity to traffic emissions during summer months.

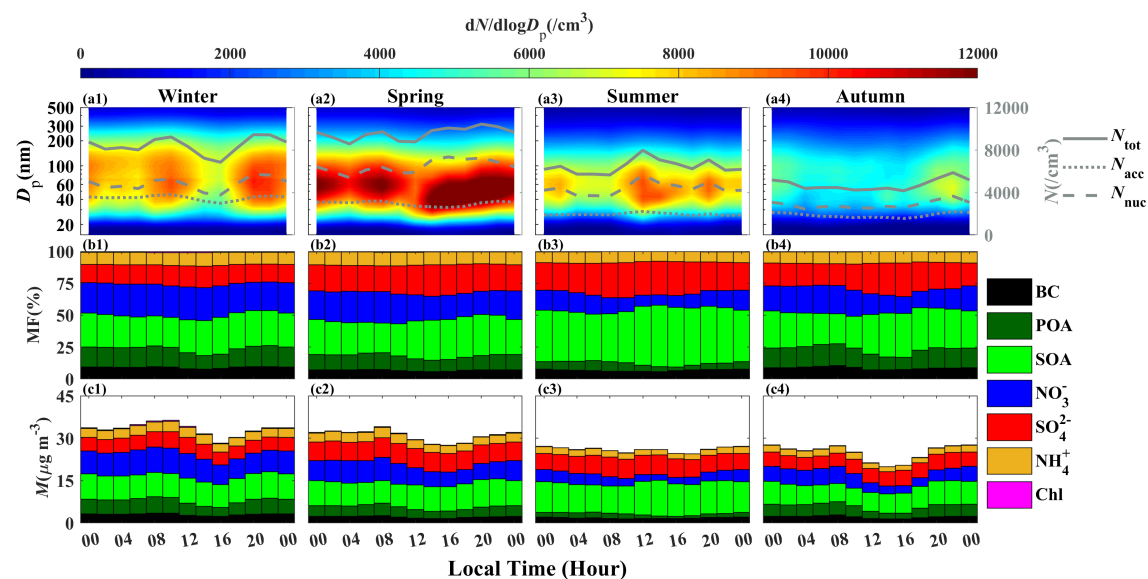


Figure 4. Diurnal variations of (a1–a4) particle number size distributions (PNSD), total particle number concentration (N_{tot}), accumulation-mode particle number concentration (N_{acc}), and nucleation-mode particle number concentration (N_{nuc}), (b1–b4) mass fractions (MF) of aerosol chemical species, and (c1–c4) mass concentrations (M) of aerosol chemical species during different seasons.

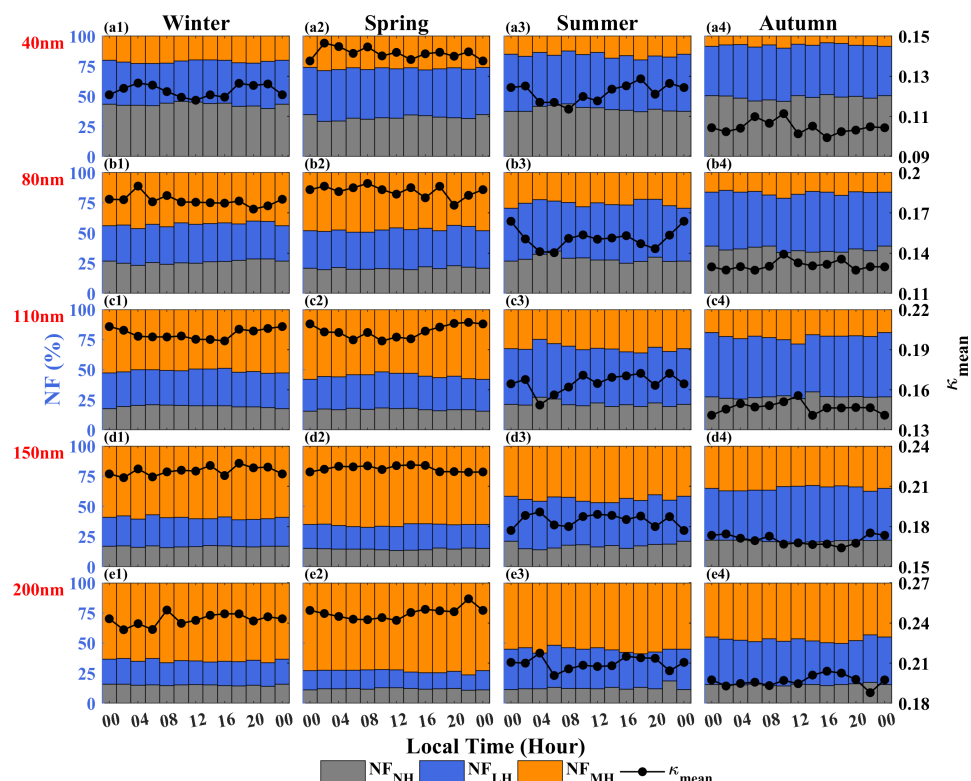


Figure 5. Diurnal variations of the NF_{MH} (orange bars), NF_{LH} (blue bars), and NF_{NH} (gray bars), and κ_{mean} (black dots) for different size particles (40–200 nm) during different seasons.

Figure 4b1–b4 reveals pronounced daytime enhancements in the mass fractions of SO_4^{2-} and SOA mass fractions across all seasons, with peak values coinciding with periods of maximum photochemical activity—a trend most pronounced in summer due to enhanced solar radiation (Peng et al., 2017). In contrast, the mass fraction of NO_3^- displays an inverse diurnal cycle, reaching maximal mass fractions during nocturnal periods. This behavior is mechanistically explained through temperature-mediated phase partitioning theory, where lower nocturnal temperatures coupled with higher relative humidity facilitate efficient gas-to-particle conversion through aqueous-phase oxidation processes (Sun et al., 2013).

These compositional shifts drive distinct hygroscopicity dynamics in accumulation-mode particles. As illustrated in Figure 5, the κ_{mean} for 200 nm particles displays a bimodal diurnal pattern due to increased NF_{MH} : a primary afternoon peak (14:00–18:00 LT), driven by photochemical production of hydrophilic SO_4^{2-} and SOA, and a secondary evening enhancement (post-20:00 LT), associated with NO_3^- accumulation under favorable nighttime chemical conditions.



3.2. Impact of NPF events on the size-resolved aerosol hygroscopicity

Figure 4a2 indicates that spring exhibits distinctive particle dynamics, characterized by frequent NPF events. The PNSD pattern displays a unique banana-shaped diurnal cycle, with the frequency of NPF occurrences reaching 20.65% during spring—approximately double the annual average and significantly higher than in other seasons (Table S2). Previous studies have shown that strong winds during prevalent spring dust episodes in China significantly scavenge fine particles, creating a cleaner environment conducive to NPF occurrence (Shen et al., 2023). In contrast to spring non-NPF days, the spring NPF days shows more pronounced diurnal fluctuations in the number concentration of nucleation-mode particles and the mass concentration of PM_{2.5} chemical compositions (Fig. S1). As shown in Fig. S1c1, around 10:00 LT in the spring NPF days, the mass concentration of PM_{2.5} sharply decreases. Under these low pollution conditions, the lower condensation sink (CS) facilitates the onset of NPF events (Hong et al., 2023). This leads to a rapid increase in N_{nuc} (Fig. S1a1).

In comparison to spring non-NPF days, MF_{OA} significantly increases in spring NPF days, with MF_{POA} gradually decreases, and MF_{SOA} gradually increases over time. This trend starts at 10:00 LT and continues until 18:00 LT to the evening rush hours (Fig. S1b1). This suggests that spring NPF events are predominantly driven by the formation of SOA. Additionally, a markedly lower κ_{mean} is observed for 40 nm particles (Fig. S2a1), suggesting that the newly formed nucleation-mode particles during NPF events exhibits lower hygroscopicity. This is related to a higher NF_{NH} and a lower NF_{MH} (Fig. S2b1 and Fig. S2d1). As the nucleation-mode particles grows, the κ_{mean} of 40 nm particles slightly increases, although it remains lower than on non-NPF days (Fig. S2).

Between 14:00–16:00 LT, the N_{nuc} reaches its peak, while the N_{acc} and the PM_{2.5} mass concentration reach their diurnal lows (Fig. S1). A distinct diurnal peak in κ_{mean} occurs around 16:00 LT for all size particles, driven by concurrent increases in both the NF_{MH} and κ_{MH} (Figs. S2 and S3). This enhancement is particularly evident for accumulation-mode particles, which have a higher NF_{MH}. These findings suggest that newly formed nucleation-mode particles, which exhibit lower hygroscopicity, gradually age and grow into more hygroscopic accumulation-mode particles over time during spring NPF days.

As shown in Figure 6a, the κ_{NH} , κ_{LH} and κ_{MH} exhibit minimal difference between NPF days and non-NPF days during spring. However, the κ_{mean} on NPF days is significantly lower by 6.76% for 40 nm particles and higher by 5.07% for 200 nm particles compared to non-NPF days (Table S3). This divergence is attributed to the changes in the NF_{NH} and NF_{MH}: NPF days have larger NF_{NH} and smaller NF_{MH} for 40 nm particles, while the opposite is observed for 200 nm particles (Figure 6b). Additionally, the diurnal variation of CV _{κ -PDF} for 40 nm particles in NPF days has obvious fluctuation, while the CV _{κ -PDF} for other particle sizes in NPF days and all particle sizes in non-NPF days has no obvious diurnal variation. This indicates that the NPF event only significantly affects the internal mixing state of small particles (40 nm particles). Furthermore, the CV _{κ -PDF} for nucleation-mode particles on NPF days is slightly larger than on non-NPF days, while the opposite is observed for accumulation-mode particles (Table S3). These findings suggest that newly formed particles during NPF events exhibit reduced internal mixing compared to non-NPF conditions, while aged larger particles demonstrate enhanced mixing homogeneity.

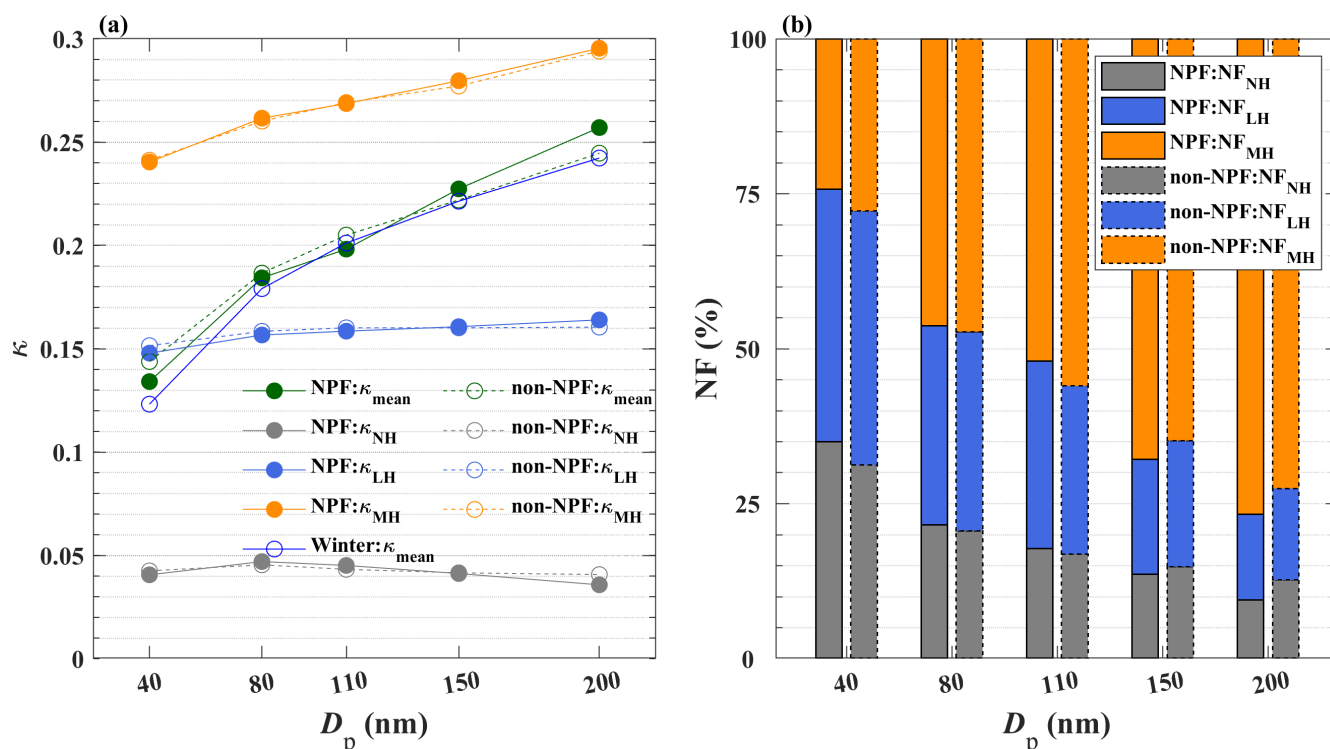


Figure 6. (a) κ_{mean} , κ_{MH} , κ_{LH} and κ_{NH} in spring NPF days and spring non-NPF days, and the κ_{mean} in winter for all size particles (40–200 nm). (b) NF_{MH}, NF_{LH}, NF_{NH} in spring NPF days and spring non-NPF days for all size particles (40–200 nm).

Similar with spring, winter exhibits the higher κ_{mean} values for particles in the 40–200 nm size range (Figure 1a). To investigate seasonal differences, the κ_{mean} values of spring NPF days and non-NPF days are compared with winter conditions (Figure 6a). For nucleation-mode particles, winter consistently shows lower κ_{mean} values than both spring NPF and non-NPF days. For accumulation-mode particles (except for 110 nm), winter κ_{mean} values are significantly lower than spring NPF days but comparable to spring non-NPF days, with only marginal differences observed. The 110 nm particles, representing a transitional size between nucleation and accumulation modes, demonstrate size-dependent behavior: during spring NPF events, their hygroscopic properties align more closely with nucleation-mode particles, resulting in lower κ_{mean} values compared to winter. In contrast, on spring non-NPF days, 110 nm particles show slightly enhanced hygroscopicity relative to winter conditions. These findings collectively demonstrate that spring NPF events serve to reduce seasonal differences in κ_{mean} for nucleation-mode particles between spring and winter, and enhance the hygroscopicity of accumulation-mode particles specifically in spring.



3.3. Impact of regional transport on aerosol hygroscopicity

3.3.1. Seasonal impacts of regional transport on aerosol hygroscopicity

Under the influence of the subtropical monsoon, seasonal variations in air mass sources are evident: while summer air masses derive from southern mountainous areas, other seasons primarily receive air masses from northern plains (Figure 7). Aerosol chemical composition analysis in different clusters (Fig. S4) shows that summer air masses contain substantially higher proportions of SOA in $PM_{2.5}$ compared to other seasons. This compositional difference leads to elevated NF_{LH} values in summer, resulting in significantly lower κ_{mean} values for accumulation-mode particles relative to winter and spring (Figure 8). Notably, springtime $PM_{2.5}$ mass concentrations show significant variation among air mass categories, with C2 exhibiting substantially lower concentrations than C1 and C3 (Fig. S4). As indicated in Table S4, the occurrence frequencies of NPF events during spring for C1, C2, and C3 are 11.16%, 42.44%, and 25.00%, respectively, demonstrating that NPF events in Nanjing preferentially occur under cleaner atmospheric conditions (lower $PM_{2.5}$ mass concentration in C2) in spring.

In contrast, autumn air masses exhibit higher POA content in $PM_{2.5}$ (Fig. S4), yielding comparable NF_{LH} but increased NF_{NH} relative to summer conditions, along with marginally reduced κ_{mean} values for equivalent particle sizes (Figure 8). While winter air masses demonstrate higher κ_{MH} (Fig. S5), spring air masses contain greater amounts of SNA in $PM_{2.5}$ (Fig. S4) and the elevated NF_{MH} ultimately produces slightly higher κ_{mean} values compared to that in winter (Figure 8). Collectively, these observations reveal that similar particle hygroscopicity under winter–spring air masses, and comparable hygroscopic properties under summer–autumn air masses (Figure 8).

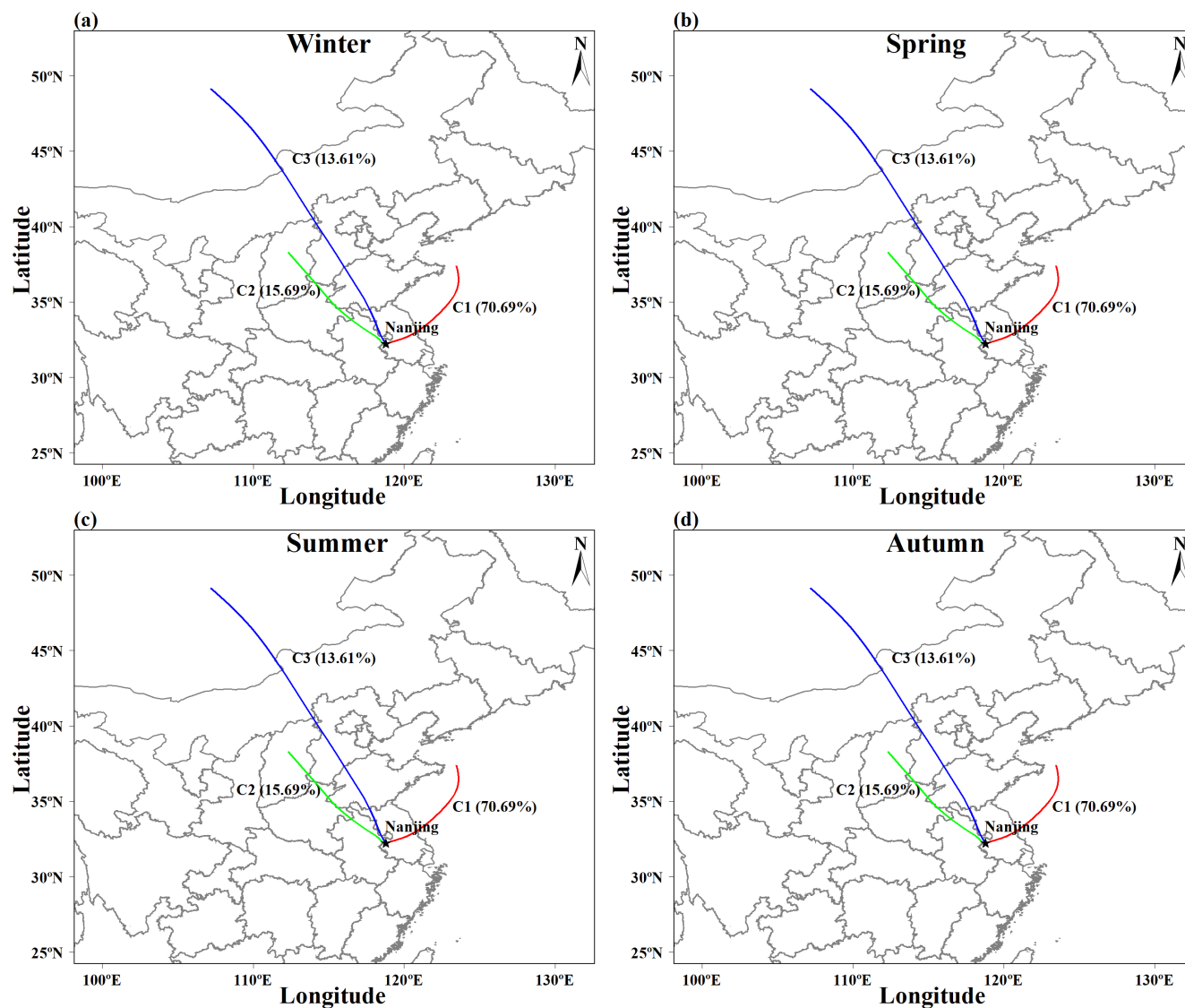


Figure 7. 72-hour air mass backward trajectories at a height of 100 meters corresponding to the cluster analysis during different seasons. The line colors denote different clusters, i.e., red for Cluster C1, green for Cluster C2, and blue for Cluster C3.

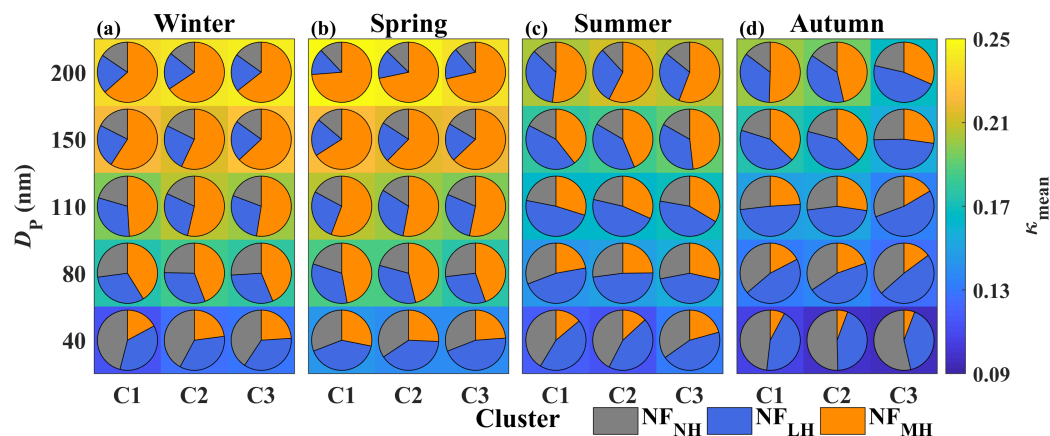


Figure 8. The κ_{mean} (color block) of aerosols and the number fractions of different hygroscopic groups for all size particles (40–200 nm) in the influence of different air masses during different seasons. The color blocks of pie chart denote number fractions of different hygroscopic groups, i.e., orange block of pie chart for NF_{MH} , blue block of pie chart for NF_{LH} , and gray block of pie chart for NF_{NH} .

3.3.2. Influence of regional transport on hygroscopicity of different mode particles

Figure 8 also demonstrates that, across all seasons except autumn, accumulation-mode particles under different air masses exhibit minimal NF variations among hygroscopicity groups within the same season. Although notable differences in κ_{MH} are observed at certain particle sizes (Fig. S5), κ_{mean} remains relatively consistent. In contrast, accumulation-mode particles during autumn display significant κ_{mean} variations across hygroscopic groups, attributable to larger NF differences despite comparable κ_{MH} values between air masses. These findings suggest that NF serves as the dominant factor governing κ_{mean} , a conclusion that aligns with the results presented in Sect.3.1.2.

Integrative examination of Figures Figure 7, Figure 8, and S4 further reveals that, within a given season, accumulation-mode particles originating from eastern/northern air masses consistently exhibit stronger hygroscopicity compared to those from western/southern sources. This enhanced hygroscopic behavior can be attributed to their higher SNA content in $\text{PM}_{2.5}$.

For nucleation-mode particles (particularly at 40 nm), κ_{mean} is predominantly influenced by NF_{NH} rather than NF_{MH} (Figure 3). Given that κ_{NH} remains relatively small and stable, seasonal variations in κ_{mean} are negligible despite substantial NF_{NH} differences across air masses (Figure 8). This implies that the hygroscopicity of nucleation-mode particles is less sensitive to air mass origins and is primarily regulated by local sources. However, an exception occurs in spring, where air masses yield significantly higher κ_{mean} values for 40 nm particles, a consequence of their elevated NF_{MH} (Figure 8).

Figure 9 shows the $\text{CV}_{\kappa\text{-PDF}}$ for size-resolved particles under varying air mass influences across seasons. Comparative analysis reveals that during non-summer seasons, 200 nm particles affected by long-range transported air masses (winter C3, spring C2, summer C2, autumn C3) demonstrate significantly higher $\text{CV}_{\kappa\text{-PDF}}$ values relative to other air masses, suggesting more



pronounced external mixing. Interestingly, summer exhibits a distinct pattern where C2-influenced 200 nm particles show even lower $CV_{\kappa\text{-PDF}}$ values compared to summer C1 and C3 cases, indicating more advanced internal mixing. This seasonal anomaly can be attributed to enhanced photochemical aging during summer transport, driven by more intensive solar radiation. Consequently, while C2-associated 200 nm particles display marginally increased hygroscopicity during summer (Figure 8c), other seasons show no statistically significant hygroscopicity enhancement in long-range transported particle clusters.

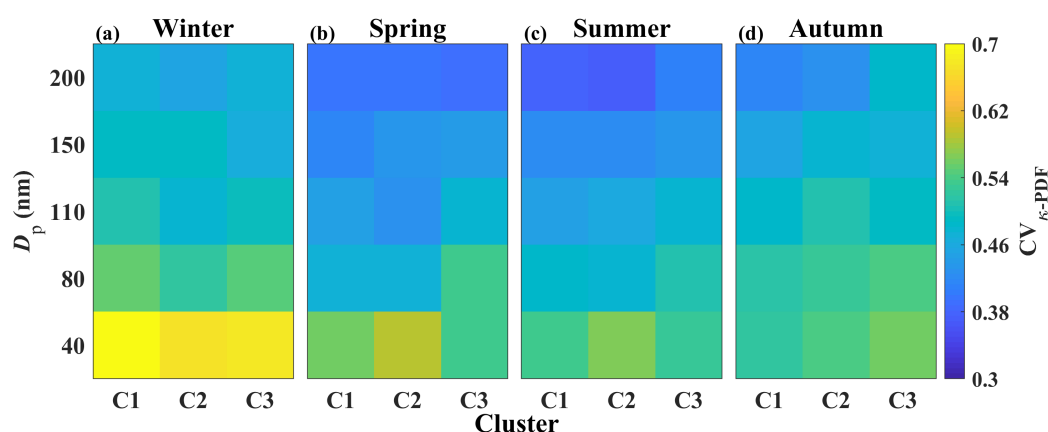


Figure 9. The $CV_{\kappa\text{-PDF}}$ for all size particles (40–200 nm) in the influence of different air masses during different seasons.

All these results reveal significantly smaller intra-seasonal hygroscopicity variations compared to inter-seasonal differences. This pattern primarily stems from more pronounced chemical composition disparities between seasonal air masses, which amplify contrasts within strongly hygroscopic particle groups. The study demonstrates distinct spatial controls on particle hygroscopicity: nucleation-mode particles exhibit predominantly local regulation, as evidenced by minimal κ_{mean} variations despite substantial NF fluctuations. In contrast, within a given season, accumulation-mode particles originating from eastern/northern air masses display enhanced hygroscopicity relative to their western/southern counterparts, attributable to elevated SNA concentrations. Notably, long-range air mass transport induces hygroscopicity enhancement exclusively during summer months for larger particles, a phenomenon driven by accelerated aging processes and more homogeneous internal mixing. No comparable effects are detected in other seasons.

4. Summary and conclusions

This study examines size-resolved and seasonal variations in aerosol hygroscopicity and their influencing factors in northern Nanjing, based on field observations at NUIST in 2021 using H-TDMA measurements.



Aerosols in this suburban region exhibit lower hygroscopicity than in other areas, primarily due to higher organic content (annual MF_{OA} in PM_{2.5}: 42.92%). The κ_{mean} increases with particle size across all seasons, especially for nucleation-mode particles. Annual κ_{mean} values (\pm standard deviations) for 40, 80, 110, 150, and 200 nm particles are 0.12 ± 0.04 , 0.16 ± 0.05 , 0.18 ± 0.05 , 0.20 ± 0.05 , and 0.22 ± 0.06 , respectively.

Winter and spring show higher κ_{mean} due to elevated levels of MF_{SNA} and stronger κ_{MH} , driven by PM_{2.5} pollution. In contrast, summer and autumn exhibit lower κ_{mean} and weaker size dependence. For nucleation-mode particles, κ_{mean} varies significantly by size in winter and spring but remains stable in other seasons. Accumulation-mode particles display weaker seasonal variation. In winter, high NO₃⁻ content boosts κ_{MH} , especially in accumulation-mode particles. However, κ_{mean} is highest in spring due to increased SNA content and NF_{MH}. Notably, 40 nm particles in spring show the highest κ_{mean} due to both increased NF_{MH} and decreased NF_{NH}.

Across all seasons, κ_{mean} is mainly governed by NF_{MH}. For nucleation-mode particles, κ_{mean} is also influenced by NF_{NH}, κ_{MH} , and κ_{LH} —particularly at 40 nm—while accumulation-mode particles are more affected by κ_{MH} . In summer and autumn, the impact of κ_{MH} diminishes, while κ_{LH} becomes more influential. Photochemical processes increase SO₄²⁻ and SOA during daytime (except winter), while NO₃⁻ accumulates at night via aqueous-phase reactions. As a result, 200 nm particles show afternoon and evening κ_{mean} peaks. Traffic emissions cause κ_{mean} dips across all sizes during morning and evening rush hours. Spring records the highest frequency of new particle formation (NPF) events (20.65%). During these events, newly formed particles are likely organic-rich, leading to lower κ_{mean} for 40 nm particles in the morning. As particles age, raising κ_{mean} for 200 nm particles by late afternoon. Compared to winter, nucleation-mode particles on spring non-NPF days and spring non-NPF days show much higher κ_{mean} , while accumulation-mode particles are similar on spring non-NPF days but significantly lower than spring NPF days (except for 110 nm). Compared to spring non-NPF days, κ_{mean} on spring NPF days decreases (by 6.76%) for 40 nm particles, and increases (by 5.07%) for 200 nm particles.

Intra-seasonal hygroscopicity variations are much smaller than inter-seasonal differences, largely due to the greater chemical contrast among seasonal air masses. Spatial controls differ by particle size: nucleation-mode particles are primarily influenced by local sources, as indicated by stable κ_{mean} despite NF variability. In contrast, within a given season, accumulation-mode particles transported from the east and north show enhanced hygroscopicity due to higher SNA levels. Notably, long-range air mass transport enhances κ_{mean} for larger particles only in summer, likely due to accelerated aging and more uniform internal mixing—an effect not observed in other seasons.

These findings provide valuable insights into the complex interactions between aerosol chemical composition, particle size, seasonal meteorological conditions, and regional air mass transport in shaping aerosol hygroscopicity. Understanding these relationships is essential for improving the accuracy of regional climate models, particularly in estimating aerosol–cloud interactions and radiative forcing. Moreover, the study highlights the critical role of local emissions and secondary processes in influencing aerosol properties, offering a scientific basis for air quality management and pollution control strategies in rapidly urbanizing regions like Nanjing and the broader Yangtze River Delta.



Data availability. Data used in the study are available at <http://gofile.me/5JhP4/wZoKYiAJn>.

445 **Author contributions.** YW designed the experiment; JZ, JX and YW carried it out and analysed the data. Other co-authors participated in science discussions and suggested analyses. JZ prepared the paper with contributions from all co-authors.

Competing interests. The authors declare that they have no conflict of interest.

450 **Acknowledgements.** This work is funded by National Natural Science Foundation of China (NSFC) research projects (Grant Nos. 42030606). We thank all participants in the field campaign for their tireless work and cooperation.



References:

- 455 Alonso-Blanco, E., Gómez-Moreno, F.J., and Artíñano, B.: Size-resolved hygroscopicity of ambient submicron particles in a suburban atmosphere, *Atmos. Environ.*, 213, 349-358, <https://doi.org/10.1016/j.atmosenv.2019.05.065>, 2019.
- Asmi, E., Frey, A., Virkkula, A., Ehn, M., Manninen, H.E., Timonen, H., Tolonen-Kivimäki, O., Aurela, M., Hillamo, R., and Kulmala, M.: Hygroscopicity and chemical composition of Antarctic sub-micrometre aerosol particles and observations of new particle formation, *Atmos. Chem. Phys.*, 10, 4253-4271, <https://doi.org/10.5194/acp-10-4253-2010>, 2010.
- 460 Chen, J., Li, Z., Lv, M., Wang, Y., Wang, W., Zhang, Y., Wang, H., Yan, X., Sun, Y., and Cribb, M.: Aerosol hygroscopic growth, contributing factors, and impact on haze events in a severely polluted region in northern China, *Atmos. Chem. Phys.*, 19, 1327-1342, <https://doi.org/10.5194/acp-19-1327-2019>, 2019.
- Chen, L., Zhang, F., Zhang, D., Wang, X., Song, W., Liu, J., Ren, J., Jiang, S., Li, X., and Li, Z.: Measurement report: Hygroscopic growth of ambient fine particles measured at five sites in China, *Atmos. Chem. Phys.*, 22, 6773-6786, <https://doi.org/10.5194/acp-22-6773-2022>, 2022.
- 465 Chen, Y., Wang, X., Dai, W., Wang, Q., Guo, X., Liu, Y., Qi, W., Shen, M., Zhang, Y., Li, L., Cao, Y., Wang, Y., and Li, J.: Particle Number Size Distribution of Wintertime Alpine Aerosols and Their Activation as Cloud Condensation Nuclei in the Guanzhong Plain, Northwest China, *J. Geophys. Res.-Atmos.*, 128, e2022JD037877, <https://doi.org/10.1029/2022JD037877>, 2023.
- 470 Draxler, R. R. and Hess, G. D.: An overview of the HYSPLIT_4 modelling system for trajectories dispersion and deposition, *Aust. Meteorol. Mag.*, 47, 295-308, 1998.
- Fan, X., Liu, J., Zhang, F., Chen, L., Collins, D., Xu, W., Jin, X., Ren, J., Wang, Y., Wu, H., Li, S., Sun, Y., and Li, Z.: Contrasting size-resolved hygroscopicity of fine particles derived by HTDMA and HR-ToF-AMS measurements between summer and winter in Beijing: the impacts of aerosol aging and local emissions, *Atmos. Chem. Phys.*, 20, 915-929, <https://doi.org/10.5194/acp-20-915-2020>, 2020.
- 475 Fors, E.O., Swietlicki, E., Svenningsson, B., Kristensson, A., Frank, G.P., and Sporre, M.: Hygroscopic properties of the ambient aerosol in southern Sweden – a two year study, *Atmos. Chem. Phys.*, 11, 8343-8361, <https://doi.org/10.5194/acp-11-8343-2011>, 2011.
- Gysel, M., Crosier, J., Topping, D.O., Whitehead, J.D., Bower, K.N., Cubison, M.J., Williams, P.I., Flynn, M.J., McFiggans, G.B., and Coe, H.: Closure study between chemical composition and hygroscopic growth of aerosol particles during TORCH2, *Atmos. Chem. Phys.*, 7, 6131-6144, <https://doi.org/10.5194/acp-7-6131-2007>, 2007.
- Hirshorn, N.S., Zuromski, L.M., Rapp, C., McCubbin, I., Carrillo-Cardenas, G., Yu, F., and Hallar, A.G.: Seasonal significance of new particle formation impacts on cloud condensation nuclei at a mountaintop location, *Atmos. Chem. Phys.*, 22, 15909-15924, <https://doi.org/10.5194/acp-22-15909-2022>, 2022.
- 485 Hong, J., Ma, J., Ma, N., Shi, J., Xu, W., Zhang, G., Zhu, S., Zhang, S., Tang, M., Pan, X., Xie, L., Li, G., Kuhn, U., Yan, C., Qi, X., Zha, Q., Nie, W., Tao, J., He, Y., Zhou, Y., Sun, Y., Xu, H., Liu, L., Cai, R., Zhou, G., Kuang, Y., Yuan, B., Wang,



- Q., Petäjä, T., Kerminen, V., Kulmala, M., Cheng, Y., and Su, H.: Low Hygroscopicity of Newly Formed Particles on the North China Plain and Its Implications for Nanoparticle Growth, *Geophys. Res. Lett.*, 51, e2023GL107516, <https://doi.org/10.1029/2023GL107516>, 2024.
- 490 Hong, J., Tang, M., Wang, Q., Ma, N., Zhu, S., Zhang, S., Pan, X., Xie, L., Li, G., Kuhn, U., Yan, C., Tao, J., Kuang, Y., He, Y., Xu, W., Cai, R., Zhou, Y., Wang, Z., Zhou, G., Yuan, B., Cheng, Y., and Su, H.: Measurement Report: Wintertime new particle formation in the rural area of the North China Plain – influencing factors and possible formation mechanism, *Atmos. Chem. Phys.*, 23, 5699-5713, <https://doi.org/10.5194/acp-23-5699-2023>, 2023.
- 495 Jiang, R., Tan, H., Tang, L., Cai, M., Yin, Y., Li, F., Liu, L., Xu, H., Chan, P.W., Deng, X., and Wu, D.: Comparison of aerosol hygroscopicity and mixing state between winter and summer seasons in Pearl River Delta region, China, *Atmos. Res.*, 169, 160-170, <https://doi.org/10.1016/j.atmosres.2015.09.031>, 2016.
- Jiang, Y., Ma, Y., Zheng, J., Ye, N., and Yuan, C.: Characterization of size-resolved aerosol hygroscopicity and liquid water content in Nanjing of the Yangtze River Delta, *J. Environ. Sci.*, 151, 26-41, <https://doi.org/10.1016/j.jes.2024.03.035>, 2025.
- 500 Jin, X., Li, Z., Wu, T., Wang, Y., Su, T., Ren, R., Wu, H., Zhang, D., Li, S., and Cribb, M.: Differentiating the Contributions of Particle Concentration, Humidity, and Hygroscopicity to Aerosol Light Scattering at Three Sites in China, *J. Geophys. Res.-Atmos.*, 127, e2022JD036891, <https://doi.org/10.1029/2022JD036891>, 2022.
- Kammermann, L., Gysel, M., Weingartner, E., and Baltensperger, U.: 13-month climatology of the aerosol hygroscopicity at the free tropospheric site Jungfraujoch (3580 m a.s.l.), *Atmos. Chem. Phys.*, 10, 10717-10732, <https://doi.org/10.5194/acp-10-10717-2010>, 2010.
- 505 Li, X., Chen, Y., Li, Y., Cai, R., Li, Y., Deng, C., Wu, J., Yan, C., Cheng, H., Liu, Y., Kulmala, M., Hao, J., Smith, J.N., and Jiang, J.: Seasonal variations in composition and sources of atmospheric ultrafine particles in urban Beijing based on near-continuous measurements, *Atmos. Chem. Phys.*, 23, 14801-14812, <https://doi.org/10.5194/acp-23-14801-2023>, 2023.
- Liu, J., Zhang, F., Xu, W., Sun, Y., Chen, L., Li, S., Ren, J., Hu, B., Wu, H., and Zhang, R.: Hygroscopicity of Organic Aerosols Linked to Formation Mechanisms, *Geophys. Res. Lett.*, 48, e2020GL091683, <https://doi.org/10.1029/2020GL091683>, 2021.
- 510 Liu, N., Cui, S., Luo, T., Chen, S., Yang, K., Ma, X., Sun, G., and Li, X.: Characteristics of Aerosol Extinction Hygroscopic Growth in the Typical Coastal City of Qingdao, China, *Remote Sens.*, 14, 6288, <https://doi.org/10.3390/rs14246288>, 2022.
- Liu, P.F., Zhao, C.S., Göbel, T., Hallbauer, E., Nowak, A., Ran, L., Xu, W.Y., Deng, Z.Z., Ma, N., Mildenberger, K., Henning, S., Stratmann, F., and Wiedensohler, A.: Hygroscopic properties of aerosol particles at high relative humidity and their diurnal variations in the North China Plain, *Atmos. Chem. Phys.*, 11, 3479-3494, <https://doi.org/10.5194/acp-11-3479-2011>, 2011.
- 515 Ma, N., Zhao, C., Tao, J., Wu, Z., Kecorius, S., Wang, Z., Größ, J., Liu, H., Bian, Y., Kuang, Y., Teich, M., Spindler, G., Müller, K., van Pinxteren, D., Herrmann, H., Hu, M., and Wiedensohler, A.: Variation of CCN activity during new particle formation events in the North China Plain, *Atmos. Chem. Phys.*, 16, 8593-8607, <https://doi.org/10.5194/acp-16-8593-2016>, 2016.



- 520 Mamali, D., Mikkilä, J., Henzing, B., Spoor, R., Ehn, M., Petäjä, T., Russchenberg, H., and Biskos, G.: Long-term observations of the background aerosol at Cabauw, The Netherlands, *Sci. Total Environ.*, 625, 752-761, <https://doi.org/10.1016/j.scitotenv.2017.12.136>, 2018.
- Müller, A., Miyazaki, Y., Aggarwal, S.G., Kitamori, Y., Boreddy, S.K.R., and Kawamura, K.: Effects of chemical composition and mixing state on size-resolved hygroscopicity and cloud condensation nuclei activity of submicron aerosols at a suburban site in northern Japan in summer, *J. Geophys. Res.-Atmos.*, 122, 9301-9318, <https://doi.org/10.1002/2017JD027286>, 2017.
- 525 Peng, C., Wang, Y., Wu, Z., Chen, L., Huang, R.J., Wang, W., Wang, Z., Hu, W., Zhang, G., Ge, M., Hu, M., Wang, X., and Tang, M.: Tropospheric aerosol hygroscopicity in China, *Atmos. Chem. Phys.*, 20, 13877-13903, <https://doi.org/10.5194/acp-20-13877-2020>, 2020.
- Peng, J., Hu, M., Du, Z., Wang, Y., Zheng, J., Zhang, W., Yang, Y., Qin, Y., Zheng, R., Xiao, Y., Wu, Y., Lu, S., Wu, Z., Guo, S., Mao, H., and Shuai, S.: Gasoline aromatics: a critical determinant of urban secondary organic aerosol formation, *Atmos. Chem. Phys.*, 17, 10743-10752, <https://doi.org/10.5194/acp-17-10743-2017>, 2017.
- 530 Petters, M.D., and Kreidenweis, S.M.: A single parameter representation of hygroscopic growth and cloud condensation nucleus activity, *Atmos. Chem. Phys.*, 7, 1961-1971, <https://doi.org/10.5194/acp-7-1961-2007>, 2007.
- Ray, A., Pandithurai, G., Mukherjee, S., Kumar, V.A., Hazra, A., Patil, R.D., and Waghmare, V.: Seasonal variability in size-resolved hygroscopicity of sub-micron aerosols over the Western Ghats, India: Closure and parameterization, *Sci. Total Environ.*, 869, 161753, <https://doi.org/10.1016/j.scitotenv.2023.161753>, 2023.
- 535 Rosenfeld, D., Sherwood, S., Wood, R., and Donner, L.: Climate Effects of Aerosol-Cloud Interactions, *Science*, 343, 379-380, <https://doi.org/10.1126/science.1247490>, 2014.
- Shen, X., Sun, J., Che, H., Zhang, Y., Zhou, C., Gui, K., Xu, W., Liu, Q., Zhong, J., Xia, C., Hu, X., Zhang, S., Wang, J., Liu, S., Lu, J., Yu, A., and Zhang, X.: Characterization of dust-related new particle formation events based on long-term measurement in the North China Plain, *Atmos. Chem. Phys.*, 23, 8241-8257, <https://doi.org/10.5194/acp-23-8241-2023>, 2023.
- 540 Shi, J., Hong, J., Ma, N., Luo, Q., He, Y., Xu, H., Tan, H., Wang, Q., Tao, J., Zhou, Y., Han, S., Peng, L., Xie, L., Zhou, G., Xu, W., Sun, Y., Cheng, Y., and Su, H.: Measurement report: On the difference in aerosol hygroscopicity between high and low relative humidity conditions in the North China Plain, *Atmos. Chem. Phys.*, 22, 4599-4613, <https://doi.org/10.5194/acp-22-4599-2022>, 2022.
- 545 Song, X., Wang, Y., Huang, X., Wang, Y., Li, Z., Zhu, B., Ren, R., An, J., Yan, J., Zhang, R., Shang, Y., and Zhan, P.: The Impacts of Dust Storms With Different Transport Pathways on Aerosol Chemical Compositions and Optical Hygroscopicity of Fine Particles in the Yangtze River Delta, *J. Geophys. Res.-Atmos.*, 128, e2023JD039679, <https://doi.org/10.1029/2023JD039679>, 2023.
- 550 Spitieri, C., Gini, M., Gysel-Beer, M., and Eleftheriadis, K.: Annual cycle of hygroscopic properties and mixing state of the suburban aerosol in Athens, Greece, *Atmos. Chem. Phys.*, 23, 235-249, <https://doi.org/10.5194/acp-23-235-2023>, 2023.



- Sun, Y., Wang, Z., Fu, P., Jiang, Q., Yang, T., Li, J., and Ge, X.: The impact of relative humidity on aerosol composition and evolution processes during wintertime in Beijing, China, *Atmos. Environ.*, **77**, 927-934, <https://doi.org/10.1016/j.atmosenv.2013.06.019>, 2013.
- 555 Svenningsson, B., Rissler, J., Swietlicki, E., Mircea, M., Bilde, M., Facchini, M.C., Decesari, S., Fuzzi, S., Zhou, J., Mønster, J., and Rosenørn, T.: Hygroscopic growth and critical supersaturations for mixed aerosol particles of inorganic and organic compounds of atmospheric relevance, *Atmos. Chem. Phys.*, **6**, 1937-1952, <https://doi.org/10.5194/acp-6-1937-2006>, 2006.
- Swietlicki, E., Zhou, J., Berg, O.H., Martinsson, B.G., Frank, G., Cederfelt, S., Dusek, U., Berner, A., Birmili, W., Wiedensohler, A., Yuskiewicz, B., and Bower, K.N.: A closure study of sub-micrometer aerosol particle hygroscopic
- 560 behaviour, *Atmos. Res.*, **50**, 205-240, [https://doi.org/10.1016/S0169-8095\(98\)00105-7](https://doi.org/10.1016/S0169-8095(98)00105-7), 1999.
- Tan, H., Yin, Y., Gu, X., Li, F., Chan, P.W., Xu, H., Deng, X., and Wan, Q.: An observational study of the hygroscopic properties of aerosols over the Pearl River Delta region, *Atmos. Environ.*, **77**, 817-826, <https://doi.org/10.1016/j.atmosenv.2013.05.049>, 2013.
- Wang, H., An, J., Cheng, M., Shen, L., Zhu, B., Li, Y., Wang, Y., Duan, Q., Sullivan, A., and Xia, L.: One year online
- 565 measurements of water-soluble ions at the industrially polluted town of Nanjing, China: Sources, seasonal and diurnal variations, *Chemosphere*, **148**, 526-536, <https://doi.org/10.1016/j.chemosphere.2016.01.066>, 2016.
- Wang, X., Shen, X.J., Sun, J.Y., Zhang, X.Y., Wang, Y.Q., Zhang, Y.M., Wang, P., Xia, C., Qi, X.F., and Zhong, J.T.: Size-resolved hygroscopic behavior of atmospheric aerosols during heavy aerosol pollution episodes in Beijing in December 2016, *Atmos. Environ.*, **194**, 188-197, <https://doi.org/10.1016/j.atmosenv.2018.09.041>, 2018.
- 570 Wang, Y., Li, Z., Zhang, R., Jin, X., Xu, W., Fan, X., Wu, H., Zhang, F., Sun, Y., Wang, Q., Cribb, M., and Hu, D.: Distinct Ultrafine- and Accumulation-Mode Particle Properties in Clean and Polluted Urban Environments, *Geophys. Res. Lett.*, **46**, 10918-10925, <https://doi.org/10.1029/2019GL084047>, 2019.
- Wang, Y., Li, Z., Zhang, Y., Du, W., Zhang, F., Tan, H., Xu, H., Fan, T., Jin, X., Fan, X., Dong, Z., Wang, Q., and Sun, Y.: Characterization of aerosol hygroscopicity, mixing state, and CCN activity at a suburban site in the central North China Plain,
- 575 *Atmos. Chem. Phys.*, **18**, 11739-11752, <https://doi.org/10.5194/acp-18-11739-2018>, 2018.
- Wang, Y., Wang, Y., Song, X., Shang, Y., Zhou, Y., Huang, X., and Li, Z.: The impact of particulate pollution control on aerosol hygroscopicity and CCN activity in North China, *Environ. Res. Lett.*, **18**, 74028, <https://doi.org/10.1088/1748-9326/acde91>, 2023.
- Wang, Y., Zhang, F., Li, Z., Tan, H., Xu, H., Ren, J., Zhao, J., Du, W., and Sun, Y.: Enhanced hydrophobicity and volatility
- 580 of submicron aerosols under severe emission control conditions in Beijing, *Atmos. Chem. Phys.*, **17**, 5239-5251, <https://doi.org/10.5194/acp-17-5239-2017>, 2017.
- Wang, Y., Zhang, R., Wang, N., Xu, J., Zhang, J., Cui, C., Lu, C., Zhu, B., Sun, Y., and Zhu, Y.: The Role of Relative Humidity in Estimating Cloud Condensation Nuclei Number Concentration Through Aerosol Optical Data: Mechanisms and Parameterization Strategies, *Geophys. Res. Lett.*, **52**, e2024GL112734, <https://doi.org/10.1029/2024GL112734>, 2025.



- 585 Wu, Z.J., Zheng, J., Shang, D.J., Du, Z.F., Wu, Y.S., Zeng, L.M., Wiedensohler, A., and Hu, M.: Particle hygroscopicity and its link to chemical composition in the urban atmosphere of Beijing, China, during summertime, *Atmos. Chem. Phys.*, 16, 1123-1138, <https://doi.org/10.5194/acp-16-1123-2016>, 2016.
- Xie, M., Feng, W., He, S., and Wang, Q.: Seasonal variations, temperature dependence, and sources of size-resolved PM components in Nanjing, east China, *J. Environ. Sci.*, 121, 175-186, <https://doi.org/10.1016/j.jes.2021.12.022>, 2022.
- 590 Yli-Juuti, T., Nieminen, T., Hirsikko, A., Aalto, P.P., Asmi, E., Hörrak, U., Manninen, H.E., Patokoski, J., Dal Maso, M., Petäjä, T., Rinne, J., Kulmala, M., and Riipinen, I.: Growth rates of nucleation mode particles in Hyytiälä during 2003−2009: variation with particle size, season, data analysis method and ambient conditions, *Atmos. Chem. Phys.*, 11, 12865-12886, <https://doi.org/10.5194/acp-11-12865-2011>, 2011.
- Zhang, F., Wang, Y., Peng, J., Ren, J., Collins, D., Zhang, R., Sun, Y., Yang, X., and Li, Z.: Uncertainty in Predicting CCN Activity of Aged and Primary Aerosols, *J. Geophys. Res.-Atmos.*, 122, 11, 711-723, 736, <https://doi.org/10.1002/2017JD027058>, 2017.
- 595 Zhang, S., Shen, X., Sun, J., Che, H., Zhang, Y., Liu, Q., Xia, C., Hu, X., Zhong, J., Wang, J., Liu, S., Lu, J., Yu, A., and Zhang, X.: Seasonal variation of particle hygroscopicity and its impact on cloud-condensation nucleus activation in the Beijing urban area, *Atmos. Environ.*, 302, 119728, <https://doi.org/10.1016/j.atmosenv.2023.119728>, 2023.

600